THE ASTRONOMICAL JOURNAL, 161:212 (15pp), 2021 May https://doi.org/10.3847/1538-3881/abe85b

Connecting Galactic Outflows and Star Formation: Inferences from Hα Maps and Absorption-line Spectroscopy at $1 \lesssim z \lesssim 1.5$*†

Nikolaus Z. Prusinski[1,2], Dawn K. Erb[1], and Crystal L. Martin[3]

[1] The Leonard E. Parker Center for Gravitation, Cosmology and Astrophysics, Department of Physics, University of Wisconsin-Milwaukee, 3135 N Maryland Avenue, Milwaukee, WI 53211, USA; nik@astro.caltech.edu, erbd@uwm.edu

[2] Cahill Center for Astronomy and Astrophysics, California Institute of Technology, MC 249-17, Pasadena, CA 91125, USA

[3] Department of Physics, University of California Santa Barbara, Santa Barbara, CA 93106, USA; cmartin@physics.ucsb.edu

Received 2020 September 28; revised 2021 January 8; accepted 2021 February 18; published 2021 April 8

Abstract

We investigate the connection between galactic outflows and star formation using two independent data sets covering a sample of 22 galaxies between $1 \lesssim z \lesssim 1.5$. The Hubble Space Telescope WFC3/G141 grism provides low spectral resolution, high spatial resolution spectroscopy yielding Hα emission-line maps from which we measure the spatial extent and strength of star formation. In the rest-frame near-UV, Keck/DEIMOS observes Fe II and Mg II interstellar absorption lines, which provide constraints on the intensity and velocity of the outflows. We compare outflow properties from individual and composite spectra with the star formation rate (SFR) and SFR surface density ($\Sigma_{\rm SFR}$), as well as the stellar mass and specific SFR (sSFR). The Fe II and Mg II equivalent widths (EWs) increase with both SFR and $\Sigma_{\rm SFR}$ at $\gtrsim 3\sigma$ significance, while the composite spectra show larger Fe II EWs and outflow velocities in galaxies with higher SFR, $\Sigma_{\rm SFR}$, and sSFR. Absorption-line profiles of the composite spectra further indicate that the differences between subsamples are driven by outflows rather than the interstellar medium. While these results are consistent with those of previous studies, the use of Hα images makes them the most direct test of the relationship between star formation and outflows at $z > 1$ to date. Future facilities such as the James Webb Space Telescope and the upcoming Extremely Large Telescopes will extend these direct, Hα-based studies to lower masses and SFRs, probing galactic feedback across orders of magnitude in galaxy properties and augmenting the correlations we find here.

Unified Astronomy Thesaurus concepts: Galaxy evolution (594); Galaxy formation (595); High-redshift galaxies (734); Starburst galaxies (1570)

1. Introduction

Galaxy evolution is driven through the baryon cycle: cool gas flows into the galaxy from the cosmic web and is converted into stars, the most massive of which quickly die, expelling their metal-enhanced baryons into the interstellar medium (ISM; Péroux & Howk 2020). These ejecta can be propelled to the circumgalactic or intergalactic media through galactic winds. Although the general outline is clear, a detailed understanding of the processes involved remains an open issue in modern astrophysics (Veilleux et al. 2020). In this study, we focus on the relationship between galactic winds and star formation.

Galaxies with intense star formation are observed to have powerful outflows of gas; however, the primary driving mechanisms remain uncertain. Active galactic nuclei (Faucher-Giguère & Quataert 2012), energy injection from supernovae (SNe; Leitherer et al. 1999; Veilleux et al. 2005), cosmic rays (Grenier et al. 2015), and radiation pressure (Murray et al. 2011) generate and sustain galactic outflows. At a given time, many of these mechanisms are occurring simultaneously, and they are likely to interact in complex and nonlinear ways that depend on the type of galaxy (Hopkins et al. 2012). These outflows transfer energy and momentum from the centers of galaxies to large radii (Chevalier & Clegg 1985; Bouche et al. 2007; Ménard et al. 2011; Murray et al. 2005). In doing so, the outflows may cause a depletion in the availability of cool gas, and star formation may be quenched (Tremonti et al. 2007; Hopkins et al. 2008; Gabor et al. 2011).

The global star formation rate (SFR) reached its peak at $z \sim 2$, and since then has been steadily decreasing (Hopkins & Beacom 2006; Bouwens et al. 2007). A decrease in the rate of cool gas accretion onto galaxies may explain this drop in star formation (Kereš et al. 2005), although a more robust understanding of galactic feedback is required to constrain the physical processes driving these changes. Simulations of feedback (e.g., Sales et al. 2010; Genel et al. 2015; Nelson et al. 2015) and how it regulates galactic disk formation (e.g., Brooks et al. 2009; Sales et al. 2012; Übler et al. 2014; Minchev et al. 2015) together with observations of gas flows at $1 < z < 2$ provide insight into galaxy and baryon cycle evolution during this critical period.

Galactic winds at $z \sim 1$ are typically traced by rest-frame UV absorption lines backlit by the stellar continuum (Weiner et al. 2009; Rubin et al. 2010; Prochaska et al. 2011; Erb et al. 2012; Kornei et al. 2012; Martin et al. 2012; Bordoloi et al. 2014). Cool ($T \sim 10^4$ K) outflowing gas appears blueshifted with respect to the systemic velocity of the galaxy. These outflows are commonplace in starburst galaxies across cosmic time, from $z \sim 0$ (Heckman et al. 1990; Strickland & Stevens 2000; Martin & Bouché 2009; Soto et al. 2012), to $z \sim 1$ (Weiner et al. 2009; Rubin et al. 2010; Zhu et al. 2015), to $z \gtrsim 2$ (Steidel et al. 2010; Shapley 2011; Schreiber et al. 2019).

---

* This work is based in part on observations taken by the 3D-HST Treasury Program (GO 12177 and 12328) with the NASA/ESA Hubble Space Telescope, which is operated by the Association of Universities for Research in Astronomy, Inc., under NASA contract NAS5-26555.

† Some of the data presented herein were obtained at the W. M. Keck Observatory, which is operated as a scientific partnership among the California Institute of Technology, the University of California, and the National Aeronautics and Space Administration. The Observatory was made possible by the generous financial support of the W. M. Keck Foundation.

Observations and simulations have suggested an SFR surface density ($\Sigma_{\rm SFR}$) threshold needed to drive outflows of $0.1\,M_\odot\,{\rm yr}^{-1}\,{\rm kpc}^{-2}$, although many factors (e.g., galaxy escape velocity, inclination angle, etc.) contribute to the presence and detectability of outflows (Heckman 2002; Murray et al. 2011; Kornei et al. 2012). Outflow velocities have been observed to increase with galaxy mass and SFR, suggesting that higher-mass galaxies have more ambient gas and energy from SNe and radiation pressure (SN rate and luminosity both scale with SFR) and therefore sustain faster outflows than their lower-mass counterparts (Martin 2005; Rupke et al. 2005; Chisholm et al. 2015). In addition, the equivalent widths of interstellar absorption lines associated with outflows are observed to increase with stellar mass, SFR, and SFR surface density (Weiner et al. 2009; Rubin et al. 2010; Martin et al. 2012; Bordoloi et al. 2014).

In this paper, we observe star formation and outflow properties for a sample of galaxies at $1 < z < 1.5$. We probe interstellar Mg II and Fe II absorption with Keck/DEIMOS and use WFC3/G141 grism data from the Hubble Space Telescope (HST) to construct Hα emission-line maps that trace the spatial distribution of star formation for each object. We determine the equivalent widths of the absorption lines along with the outflow velocities of the gas flows. SFR surface densities for the same objects are ascertained through area measurements of the highest surface brightness regions of the Hα maps. By combining the two data sets, we directly compare the structure of star formation to the outflow properties.

The paper is organized as follows. We describe the joint data set in Section 2. Section 2.1 shows how Hα emission-line maps were constructed, Section 2.1.1 explains how SFR surface densities were calculated, and Section 2.2 shows how outflow properties were measured. In Section 3, we discuss the correlations between star formation and outflow properties. In Section 3.1, we form composite absorption-line spectra, and in Section 4, we summarize and discuss our results. Throughout this paper, we use the Salpeter (1955) IMF and adopt the Planck Collaboration et al. (2016) cosmology with $H_0 = 67.74$ km s^{-1} Mpc^{-1}, $\Omega_m = 0.3089$, and $\Omega_\Lambda = 0.6911$. In this cosmology, at the median redshift of the sample ($z = 1.22$), 1″ corresponds to 8.5 kpc.

2. Observations, Data Reduction, and Measurements

In order to measure star formation and outflow velocities at $1 \lesssim z \lesssim 1.5$, we constructed a joint data set comprising rest-frame near-UV absorption-line spectra and rest-frame optical grism spectra to measure emission lines. Keck/DEIMOS detected Fe II and Mg II absorption lines which provided outflow velocities, and the Hα emission line observed with HST WFC3/G141 traces star formation.

The galaxies in this sample were selected from the Cosmic Assembly Near-IR Deep Extragalactic Legacy Survey (CANDELS), specifically the Extended Groth Strip (EGS; α = 14:19:31, δ = +52:51:00) and the Cosmic Evolution Survey (COSMOS; α = 10:00:29, δ = +02:20:36) fields (Grogin et al. 2011; Koekemoer et al. 2011). The sample was chosen using data from the Skelton et al. (2014) photometric catalog such that each galaxy had (1) an ${\rm SFR} > 1\,M_\odot\,{\rm yr}^{-1}$ as measured by spectral energy distribution (SED) fitting from the photometric catalog; (2) $0.7 \lesssim z_{\rm phot} \lesssim 1.6$ at 99% confidence so that the systemic redshift $z_{\rm sys}$ could be measured from the [O II] $\lambda\lambda$3727, 3729 doublet, and absorption lines from Fe II (∼2300–2600 Å) and Mg II (2800 Å) were visible; and (3) $\mathcal{R} \lesssim 24$ in order to obtain spectra with a continuum signal-to-noise ratio (S/N) sufficient to measure absorption lines in individual objects in one night of observation. Starting from the full COSMOS and EGS catalogs, we eliminated objects with unreliable photometry or poorly constrained SED fits, which when combined with the above three criteria reduced the 29,791 (36,699) objects in the COSMOS (EGS) field to a sample of 520 (446) galaxies. Of the three requirements, the magnitude cut eliminated the largest number of objects from the sample. Because our targets are bright, the catalog from which they are drawn is highly complete over our magnitude range of interest; Skelton et al. (2014) estimate a 90% completeness level at $H_{\rm F160W} = 25.1$, while the faintest object in our final sample is two magnitudes brighter than this with $H_{\rm F160W} = 23.1$. We therefore expect our parent sample to be highly complete, but note that our selection criteria may eliminate dusty galaxies with ${\rm SFR} > 1\,M_\odot\,{\rm yr}^{-1}$ but $\mathcal{R} > 24$.

Ground-based observations for 84 of these galaxies were conducted on 2015 March 26 and 27 using the DEep Imaging Multi-Object Spectrograph (DEIMOS) on the Keck II telescope. DEIMOS is a medium-resolution optical spectrometer with spectral coverage from 4000 to 10500 Å (Faber et al. 2003). Out of the 84 galaxy sample at $1 < z < 1.5$, 47 objects had significant absorption-line detections. These lines include Fe II λ2344, λ2374, λ2383, λ2587, λ2600, and Mg II $\lambda\lambda$2796, 2804, which trace the outflow velocities of interstellar gas. DEIMOS observations were conducted using the 600 lines mm^{-1} grating with one slitmask per field and 1″ slits. The dispersion was 0.65 Å pixel^{-1} and the spectral resolution FWHM was 4.6 Å or ∼180 km s^{-1} as measured from the widths of night sky lines. Total exposure times for the EGS and COSMOS fields were 8.79 hr and 9.04 hr respectively. The airmass ranged between 1.05 and 1.31, and the average seeing was ∼0.″6.

We further restrict our study to objects with detections of Hα emission in the 3D-HST grism survey (van Dokkum et al. 2011; Brammer et al. 2012; Momcheva et al. 2016). Each of the galaxies in the EGS and COSMOS fields has WFC3 F140W+G141 direct and grism observations from two visits with an average exposure time of ∼5600 s. The F140W filter and G141 grism have overlapping wavelength coverage from ∼12000 to 16000 Å, with Hα visibility from $z \sim 0.75$ to $z \sim 1.5$ (2.75 Gyr of cosmic time). Excluding objects with strong contamination (shown in Figure 2 and discussed in Section 2.1) and retaining objects with significant Hα emission and either Fe II or Mg II absorption-line detections led to a final sample of 22 galaxies (14 in COSMOS and 8 in EGS). Of those 22 objects, 18 have significant Fe II detections, 20 have significant Mg II detections, and 16 have detections of both Mg II and Fe II absorption features. The median redshift of the sample is 1.22 with standard deviation 0.16, and the galaxies generally fall on the star-forming main sequence for that redshift (Speagle et al. 2014).

Figure 1 shows the range of galaxy physical parameters for the 22 object sample. We observe a median stellar mass (M_*) of $1.1 \times 10^{10}\,M_\odot$, a median SFR of $10.6\,M_\odot\,{\rm yr}^{-1}$, a median specific SFR (sSFR) of 1.0 Gyr^{-1}, and a median SFR surface density of $0.4\,M_\odot\,{\rm yr}^{-1}\,{\rm kpc}^{-2}$.

2.1. Rest-frame Optical Data from HST

The HST/WFC3 grism images were reduced using the Grism Redshift and Line Analysis (`Grizli`[4]) pipeline (see Brammer 2019; Wang et al. 2019; Abramson et al. 2020 for

---

[4] https://github.com/gbrammer/grizli/

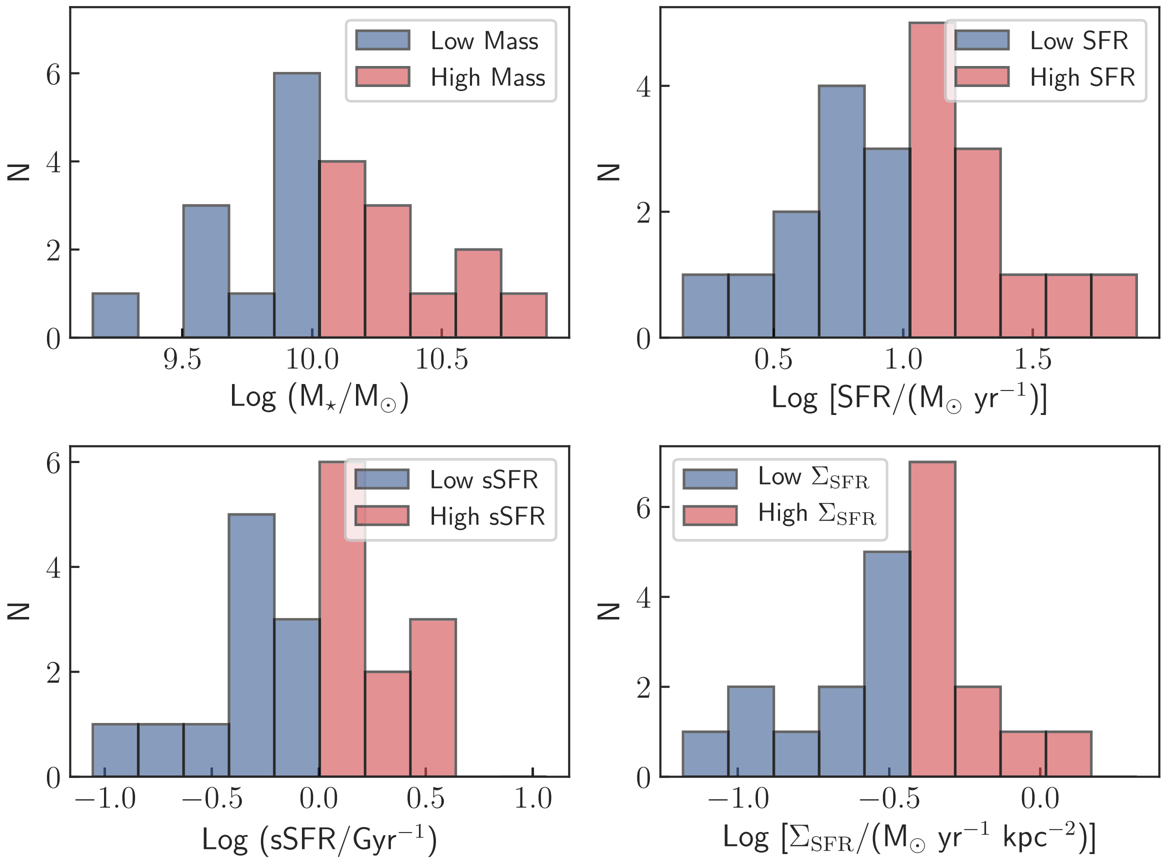

Figure 1. Distributions of galaxy properties for the 22 galaxy sample. Stellar mass (top left), star formation rate (top right), specific star formation rate (bottom left), and star formation rate surface density (bottom right) are shown. As described in Section 3.1, the full sample is split into two 11 object subsamples based on the median value of a given parameter. The blue and red histograms correspond to the low and high subsamples, respectively, from which composite spectra are formed.

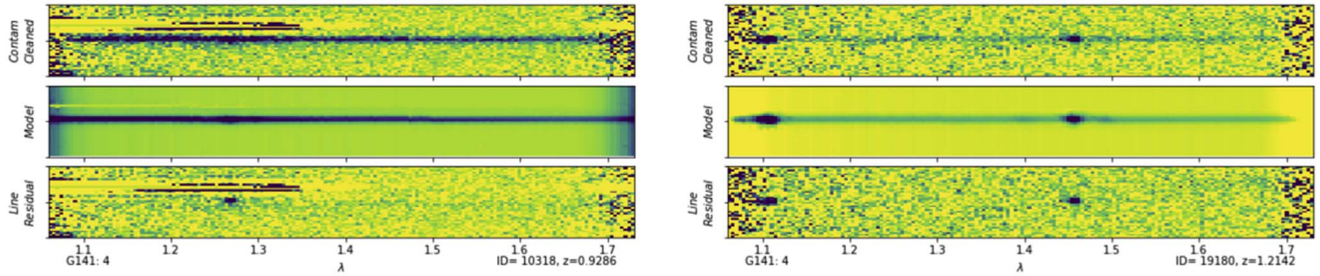

Figure 2. Examples of 2D spectra taken by the WFC3/G141 grism on HST. The `Grizli` pipeline produces a fully reduced 2D spectrum (top panel) and model (middle panel), and subtracts the continuum to produce a line-only spectrum (bottom panel). On the left, COS 10318 has Hα emission visible at 1.27 μm, while COS 19180 (right) has [O III] and Hα emission lines present at 1.11 and 1.45 μm, respectively. The dark bands in the spectrum of COS 10318 are contamination from another source in the field also visible in the Hα map in Figure 3.

descriptions of `Grizli`). We input WFC3 direct images paired with G141 grism images containing dispersed 2D spectra for each of the objects in the field. In addition, we supply the spectroscopic redshift of the target galaxy given by the [O II] emission line observed in the Keck/DEIMOS spectra. `Grizli` first preprocesses the G141 exposures by performing astrometric alignment, background subtraction, flat-fielding, and extracting visit-level catalogs and segmented images from the corresponding direct image. Using the `AstroDrizzle` software (Gonzaga 2012), the pipeline returns drizzled mosaics of the direct and grism images. `Grizli` then makes continuum and contamination models using a polynomial fit and extracts 1D and 2D spectra. Examples of the 2D spectra are shown in Figure 2.

The next step is the creation of Hα emission-line maps. These are possible because of WFC3's high spatial resolution ($0\farcs136$) and G141's low ($R \sim 130$) point-source spectral resolution. A G141 grism spectrum comprises high spatial resolution images placed in series on the WFC3 detector in 46 Å increments. These exposures cover the wavelength range (1075–1700 nm) of G141 and are placed sequentially on the WFC3 detector. To make the emission-line maps, a spectral template is fit to the data using the given spectroscopic redshift of the galaxy. The maps are constructed by subtracting the stellar continuum model from the 2D spectrum; the remaining flux comes from emission features (Nelson et al. 2016a). The direct image is used to map the spatial distribution of the emission line from the 2D spectrum to an 80 × 80 pixel postage

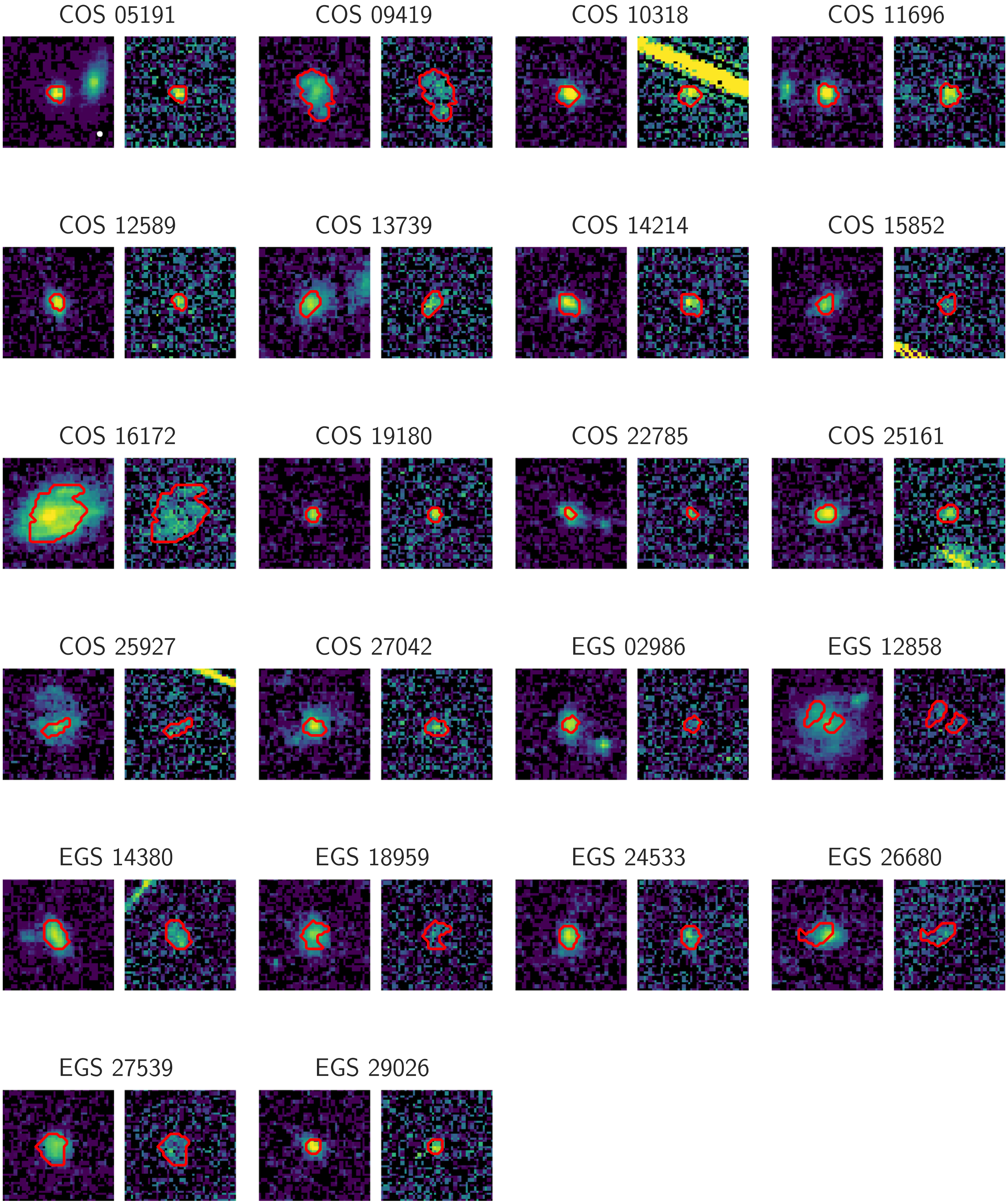

Figure 3. F140W direct images (left panel) and Hα line maps (right panel) of the objects in the sample. Each image is $4''$ on a side with the red contour indicating the area maximizing the Hα S/N. The WFC3/G141 PSF has an FWHM of $0\farcs136$ and is denoted by the white circle in the top-left plot. All plots are on a log color scale. The direct images have a scale ranging between 5×10^{-22} and 2×10^{-20} erg s^{-1} cm^{-2} Å^{-1} while the Hα emission-line maps have a scale between 5×10^{-19} and 1×10^{-17} erg s^{-1} cm^{-2}.

stamp. With the pixel scale of $0\farcs1$, this corresponds to $8'' \times 8''$ or 68×68 kpc at $z = 1.22$. In Figure 3, we plot the central $4'' \times 4''$ region of each Hα emission-line map. The emission line in these maps appears as an image of the galaxy taken at the wavelength of the line. Some of these images contain contamination from other spectra in the field (see left panel of Figure 2). We retained objects for which we were able to exclude regions with strong contamination, so that the contamination did not significantly impact the flux from the Hα line.

We apply two corrections to the Hα flux in these maps: a [N II] correction and an extinction correction. Due to the low spectral resolution of the G141 grism, the Hα and [N II] λ 6583 lines are blended, so we observe the combined flux of the two lines. After converting the galaxy masses in the photometric catalog (Skelton et al. 2014) to a Salpeter (1955) IMF, we estimate the [N II] emission as a function of galaxy mass using the [N II]/Hα mass–metallicity relation from Yabe et al. (2014). We then subtract the estimated [N II] contribution from the total observed flux. The median [N II] contribution across the sample is ∼17% of the total flux. For the extinction correction, we assume the Calzetti et al. (2000) extinction law and use A_V values from the photometric catalog to apply an extinction correction to each of the Hα fluxes; the median Hα flux correction factor is 1.52.

We note that the adoption of a single value for A_V assumes that the extinction does not vary across the galaxy, which may not be the case (e.g., Wang et al. 2017); however, the fact that we focus only on the central regions with the highest surface brightness Hα emission likely mitigates this effect. It is also probable that the value of A_V determined from the SED fitting of the spatially integrated stellar continuum is not the value appropriate for the strongest Hα emission, because nebular emission is generally more attenuated than the continuum (Calzetti et al. 2000; Reddy et al. 2015), and extinction gradients measured from the Balmer decrement tend to peak in the centers of galaxies (Nelson et al. 2016b). Because our galaxy sample does not have Hβ emission measured over the same regions as Hα, we are unable to quantify this effect, but the potential impact is that the extinction corrections are underestimated, and therefore, the SFRs and SFR surface densities may be higher than reported.

2.1.1. *Calculation of Star Formation Rate Surface Densities*

With dust and [N II]-corrected Hα fluxes in hand, we now seek to measure the galaxy area and compute SFR surface densities. Many previous studies (e.g., Rubin et al. 2010; Bordoloi et al. 2014; Heckman et al. 2015; Heckman & Borthakur 2016) have used an area proportional to πr^2, where r is the half-light radius measured from space-based rest-frame UV imaging. Others have made minor variations to this method such as using the galaxy's semimajor axis (Rubin et al. 2014) as opposed to the half-light radius; however, because star formation often occurs in small, separated clumps, sizes measured in this way may overestimate the area of the regions most likely to produce outflows (Rubin et al. 2010).

Kornei et al. (2012) take a more refined approach to measuring the SFR surface density, targeting regions of a galaxy with active star formation. For the subset of their sample in the redshift range for which the Kennicutt (1998) conversion between UV luminosity and star formation can be applied, they calculate a "clump" area by selecting pixels above a $\Sigma_{\rm SFR}$ threshold of $0.1\,M_\odot\,{\rm yr}^{-1}\,{\rm kpc}^{-2}$, because these are most likely to contribute to driving outflows. They then parameterize this area measurement by calculating a scale factor between the "clump" area and the area calculated using $\pi r_{\rm P}^2$, where $r_{\rm P}$ is the Petrosian radius. They find that the median "clump" area is 74% of the area corresponding to the Petrosian radius, and then systematically define the area of each object to be the brightest region of the galaxy containing 74% of the flux within the Petrosian radius.

Because our study has the advantage of using Hα images, we can define areas that directly measure the regions of strongest star formation by converting the Hα luminosity of each pixel to SFR via the Kennicutt (1998) relation. On the other hand, the Hα emission-line maps have much lower S/N than the broadband images used to measure sizes in previous studies, and the S/N of individual pixels with $\Sigma_{\rm SFR} \sim 0.1\,M_\odot\,{\rm yr}^{-1}\,{\rm kpc}^{-2}$ is generally low (∼1). For several reasons, we opt not to simply measure the area corresponding to the pixels above a specified SFR surface density threshold as suggested by Kornei et al. (2012). First, although there is some observational and theoretical justification for a threshold of $\Sigma_{\rm SFR} = 0.1\,M_\odot\,{\rm yr}^{-1}\,{\rm kpc}^{-2}$, this value is not robustly determined, and we therefore prefer not to impose a somewhat arbitrary threshold onto the data. The use of a constant threshold also does not take the varying noise properties of the images into account, and because the S/N of the pixels near the proposed threshold is low, it also results in the inclusion of significant noise.

Instead of using pixels above a particular threshold, we adopt a technique motivated by aperture photometry and define an optimal Hα aperture designed to maximize the S/N of the integrated flux. In the case of background-dominated observations, the radius that maximizes the S/N of the enclosed flux is directly related to the characteristic scale of the surface brightness profile; for an exponential profile, the optimal radius is $1.8h$, where h is the scale length, while for a Gaussian profile, it is 1.6σ or 0.67 FWHM (see the Appendix for a derivation).

We iteratively determine this optimal region by smoothing the emission line and error images slightly, using a range of smoothing kernels (typically 12 pixels). For each smoothed image, we create a series of apertures of varying sizes by selecting the pixels falling above a range of S/N thresholds in the smoothed data and then measure the enclosed flux and its uncertainty for each of these apertures on the original, unsmoothed images. Finally, we choose the aperture that maximizes the Hα S/N in the original data. As expected, this method tracks the highest surface brightness regions but has the advantages of not imposing a semiarbitrary SFR surface density threshold and still allowing fainter pixels to contribute. We find that the median aperture size resulting from this method matches that found by instead including all pixels above a threshold of $\Sigma_{\rm SFR} > 0.18\,M_\odot\,{\rm yr}^{-1}\,{\rm kpc}^{-2}$, although not all pixels within our apertures are above this threshold. The optimal Hα apertures are shown by red contours in Figure 3. For comparison, these apertures are 40%–90% of the galaxy sizes measured from the direct F140W images by the `Grizli` pipeline. As a result, Hα fluxes measured using the full-light apertures from the direct images are ∼1.4 times larger than those of the maximal S/N method.

Once the sizes of the Hα regions are defined, we convert the Hα luminosity within each aperture to the SFR of the galaxy using the Kennicutt (1998) relation and find the SFR surface density by dividing the SFR by the area of the aperture. We note that there is a systematic uncertainty associated with the conversion of Hα luminosity to SFR, which Kennicutt (1998) estimated to be ∼30% from the variation in other published models and calibrations at the time. The resulting median $\Sigma_{\rm SFR}$ for the 22 galaxy sample is $0.4\,M_\odot\,{\rm yr}^{-1}\,{\rm kpc}^{-2}$; this is higher than that of Kornei et al. (2012) because the lower-S/N Hα images are less effective in tracing fainter star formation. However, our sample spans more than an order of magnitude in $\Sigma_{\rm SFR}$, and we also find that four objects have an SFR surface

Table 1

Galaxy Masses and Star Formation Rates

Object	$z_{\rm sys}$[a]	M_*[b] ($10^9\,M_\odot$)	SFR[c] ($M_\odot$ yr^{-1})	sSFR[c] (Gyr^{-1})	$\Sigma_{\rm SFR}$[c] ($M_\odot$ yr^{-1} kpc^{-2})
COS 05191	1.22457 ± 0.00004	5.2 ± 0.8	15.0 ± 1.8	2.88 ± 0.76	0.76 ± 0.07
COS 09419	1.32996 ± 0.00002	14.3 ± 3.1	30.2 ± 5.7	2.11 ± 0.86	0.28 ± 0.06
COS 10318	0.92615 ± 0.00002	8.6 ± 1.9	11.4 ± 2.9	1.32 ± 0.62	0.42 ± 0.12
COS 11696	1.51683 ± 0.00004	21.6 ± 2.7	38.4 ± 3.1	1.77 ± 0.37	1.18 ± 0.07
COS 12589	1.07264 ± 0.00001	4.5 ± 1.0	6.5 ± 1.9	1.45 ± 0.75	0.43 ± 0.07
COS 13739	1.21423 ± 0.00001	10.6 ± 0.7	10.8 ± 1.9	1.02 ± 0.24	0.34 ± 0.05
COS 14214	1.40351 ± 0.00002	7.2 ± 1.4	19.7 ± 3.7	2.75 ± 1.05	0.57 ± 0.13
COS 15852	1.18903 ± 0.00001	3.9 ± 0.6	5.1 ± 1.2	1.30 ± 0.50	0.23 ± 0.02
COS 16172	1.03018 ± 0.00006	73.3 ± 21.6	76.3 ± 7.4	1.04 ± 0.41	0.38 ± 0.04
COS 19180	1.21327 ± 0.00001	2.0 ± 0.1	5.9 ± 0.6	2.97 ± 0.45	0.42 ± 0.04
COS 22785	1.23736 ± 0.00002	3.8 ± 0.7	3.0 ± 2.0	0.80 ± 0.68	0.37 ± 0.08
COS 25161	1.12831 ± 0.00001	10.8 ± 2.5	10.8 ± 2.1	1.00 ± 0.42	0.43 ± 0.06
COS 25927	1.40368 ± 0.00004	14.6 ± 3.2	8.0 ± 2.2	0.55 ± 0.27	0.30 ± 0.03
COS 27042	1.49868 ± 0.00004	24.3 ± 1.9	18.1 ± 3.2	0.74 ± 0.19	0.67 ± 0.06
EGS 02986	1.09698 ± 0.00002	10.1 ± 1.5	2.1 ± 1.0	0.20 ± 0.13	0.13 ± 0.02
EGS 12858	1.10386 ± 0.00001	35.9 ± 9.7	3.2 ± 1.1	0.09 ± 0.05	0.07 ± 0.01
EGS 14380	1.07581 ± 0.00005	23.7 ± 6.8	10.4 ± 2.7	0.44 ± 0.24	0.23 ± 0.05
EGS 18959	1.39209 ± 0.00002	19.3 ± 3.4	6.4 ± 1.8	0.33 ± 0.15	0.15 ± 0.02
EGS 24533	1.28145 ± 0.00001	9.9 ± 3.8	11.5 ± 3.3	1.16 ± 0.78	0.37 ± 0.06
EGS 26680	1.06009 ± 0.00004	10.6 ± 1.6	4.7 ± 1.5	0.44 ± 0.21	0.11 ± 0.02
EGS 27539	1.50368 ± 0.00010	44.2 ± 12.5	21.4 ± 5.6	0.48 ± 0.26	0.34 ± 0.07
EGS 29026	1.28263 ± 0.00002	15.3 ± 5.4	7.8 ± 2.3	0.51 ± 0.33	0.48 ± 0.08

Notes.

[a] Systemic redshift ($z_{\rm sys}$) from [O II] $\lambda\lambda$3727, 3729 measured by Keck/DEIMOS.

[b] Stellar masses (M_*) from the 3D-HST photometric catalog (Skelton et al. 2014) with uncertainties from R. Skelton (2021, private communication), converted to a Salpeter (1955) IMF.

[c] Star formation rates (SFR), specific star formation rates (sSFR), and star formation rate surface densities ($\Sigma_{\rm SFR}$) computed from HST WFC3/G141 Hα emission-line maps (see Figure 3).

density less than $0.18\,M_\odot$ yr^{-1} kpc^{-2}, and one (EGS 12858) has $\Sigma_{\rm SFR} < 0.1\,M_\odot$ yr^{-1} kpc^{-2}.

For comparison with the literature, we also calculate SFR surface densities using the methodology of Bordoloi et al. (2014), who adopt SFRs from SED fitting and define the SFR surface density to be $\Sigma_{\rm SFR,B} = {\rm SFR}/2\pi R_{1/2}^2$, where $R_{1/2}$ is the half-light radius. Using SFRs from the Skelton et al. (2014) photometric catalog and half-light radii from the measurements of van der Wel et al. (2012), we find that the median SFR surface densities corresponding to our optimal apertures are a factor of ∼1.8 times larger than the values of $\Sigma_{\rm SFR,B}$ for the sample. We discuss how correlations between these SFR surface densities and our outflow-related quantities compare with the optimal aperture results in Section 3.

The sSFR of each galaxy is computed by dividing the SFR by the stellar mass determined from the SED in the 3D-HST catalog (Skelton et al. 2014). Uncertainties on the stellar mass and A_V are provided by R. Skelton (2021, private communication), which we propagate into our error calculations below. To establish uncertainties on each of our measured parameters, 350 Monte Carlo simulations were run for each galaxy. Each pixel in the emission-line map was perturbed by a random amount drawn from a Gaussian distribution of width equal to the uncertainty on that pixel, and the measurements of area and SFR described above were repeated on each perturbed Hα image. The error for each quantity was then estimated from the width of the 68% confidence interval in the resulting distributions. The resulting measurements and uncertainties are given in Table 1.

2.2. Rest-frame Near-UV Keck Spectroscopy

The Keck/DEIMOS spectra were reduced using the DEEP2 reduction pipeline (Cooper et al. 2012; Newman et al. 2013),[5] which produces one-dimensional air wavelength-calibrated galaxy, inverse variance, and sky spectra. We then refined the wavelength calibration using the night sky lines, removed the instrumental signature using standard stars observed on the same night as the science data, and rebinned the spectra by a factor of 2 to increase the S/N; see Erb et al. (2012) for more details. The final spectra have a median S/N of 7.6 per resolution element over the wavelength range for which we measure absorption features.

We measured systemic redshifts for the sample of 22 galaxies by fitting a double Gaussian to the [O II] $\lambda\lambda$3727, 3729 emission lines, and then shifted the spectra to the rest frame. We normalized the spectra over the wavelength range 2300–2850 Å, as this interval contains the Fe II and Mg II spectral features of interest. Following a slight modification of the procedure outlined by Rix et al. (2004), we defined a series of continuum windows and fit a spline curve to the median fluxes in each of the windows. Each spectrum was then divided by the best fit to its continuum. The uncertainty on the points to be fit was defined as the standard deviation of the mean of the fluxes in each window. For a conservative estimate of the uncertainty associated with the continuum fit, we also calculated a high (and low) continuum fit by adding (subtracting) the continuum uncertainties to the median fluxes in each window. The adopted uncertainties on the

---

[5] https://www2.keck.hawaii.edu/inst/deimos/pipeline.html

continuum fits are then half of the range between the high and low continuum fits, and are typically ≈ ±4% across the sample. The continuum-normalized spectra were used for the analysis that follows.

We then measured the equivalent widths (EWs), velocity centroids (Δv), and maximum blueshifted velocities ($v_{\rm max}$) for all of the absorption lines of interest. EWs are measured by direct integration over the region for which the flux is below the continuum, and the maximum blueshifted velocity is defined as the velocity corresponding to the wavelength where the absorption feature first meets the continuum on the blue side of the line. Uncertainties in each of these quantities were determined from the 68% confidence intervals of 1000 Monte Carlo simulations.

Defining a detection as a $\geqslant 3\sigma$ measurement of the equivalent width, we detect at least one Fe II line in 18 galaxies (typically Fe II λ2600, detected in 17 of 18 sources with Fe II detections). Fifteen of those 18 objects have at least two Fe II lines detected, with both Fe II λ2587 and Fe II λ2600 detected in 13 of the 15 objects with two or more Fe II detections. In four galaxies, we detect some or all of the bluer lines (Fe II λ2344, λ2374, λ2383) in addition to Fe II λ2587 and Fe II λ2600. For the Mg II $\lambda\lambda$2796, 2804 absorption system, Mg II λ2796 is detected in 20 objects, and 17 of those 20 have 3σ detections of both lines. Representative examples of the spectra are shown in Figure 4.

The commonly detected interstellar absorption lines in star-forming galaxies at $z \gtrsim 1$ are typically strongly saturated, such that the EW is largely determined by the covering fraction and velocity range of the absorbing gas (e.g., Shapley et al. 2003; Erb et al. 2012). In addition, the ISM and outflow components of the absorption features are blended at the resolution of our spectra; we discuss this further in Section 3.1 when looking at the line profiles of composite spectra. We confirm that for a given object, the Fe II EWs are generally consistent within the uncertainties, indicating that the lines are indeed saturated. We therefore adopt a weighted average of the EWs and velocities of the detected Fe II features, using the inverse variance of each measurement as the weight and the inverse of the square root of the sum of the weights as the uncertainty in the average. For Mg II, we use only the Mg II λ2796 line for EW and velocity calculations, because the blue side of Mg II λ2804 is often blended with Mg II λ2796. EW and velocity measurements from the DEIMOS spectra are shown in Table 2.

3. Results

The complete sample of objects is shown in Figure 3, with F140W direct images (left) and Hα emission-line maps (right) for each galaxy. The area that maximizes the S/N of the integrated Hα flux is overplotted with a red contour. We find that the regions of strongest star formation are not necessarily contiguous (e.g., EGS 12858), and distinct regions with higher Hα surface densities may exist away from the center. From the 22 object sample, 21 objects have $\Sigma_{\rm SFR} > 0.1\,M_\odot\,{\rm yr}^{-1}\,{\rm kpc}^{-2}$, with a median SFR surface density of $0.37\,M_\odot\,{\rm yr}^{-1}\,{\rm kpc}^{-2}$.

We test for the presence of outflows or inflows by determining whether the centroids of the Fe II absorption lines are consistent with the systemic velocity. At the 1σ level, 14 objects have outflows and 3 have inflows, while the remaining 5 objects have velocity offsets consistent with zero. Requiring a 3σ threshold results in six objects with outflows and no inflows. Kolmogorov–Smirnov tests indicate that each of these subsamples is consistent with being drawn from the same parent distribution in terms of stellar mass, SFR, and SFR surface density. We use the Fe II centroid velocities because the Fe II absorption lines are less susceptible to emission-line filling. For the four galaxies with Fe II nondetections, we use the Mg II λ2796 centroid instead. Four of the six objects with 3σ detections of outflows are measured with Fe II, indicating that outflow detections are not dominated by the effects of Mg II emission-line filling.

In Figures 5–7, we compare the stellar mass, SFR, sSFR, and $\Sigma_{\rm SFR}$ against EW, Δv, and $v_{\rm max}$, respectively, for all objects in the data set. We test for correlations using the Spearman correlation coefficient, ρ, and determine the significance, σ, which represents the number of standard deviations from the null hypothesis (no correlation between quantities). We find that the strength of Fe II and Mg II absorption increases with the SFR surface density: both the Fe II and Mg II EWs are correlated with $\Sigma_{\rm SFR}$ at the 3.4σ level, with similar correlation coefficients of $\rho = 0.73$ and $\rho = 0.69$, respectively.

We also find that the Mg II equivalent width is positively correlated ($\rho = 0.67$) with the SFR at the 3.2σ level. In addition, the Fe II EW has a marginal correlation ($\rho = 0.65$, $\sigma = 2.9$) with the SFR. These correlations suggest that galaxies with more star formation drive more gas to a broader range of velocities, thereby increasing the EW of the absorption lines. Finally, we find a weak correlation between Mg II maximum outflow velocity and the SFR surface density ($\rho = -0.59$), with 2.7σ significance. We find no correlations between between outflow velocity and the sSFR, nor any correlations between stellar mass and EW or outflow velocity.

For a more direct comparison with the literature, we test the SFR surface densities $\Sigma_{\rm SFR,B}$ computed using the Bordoloi et al. (2014) method (discussed in Section 2.1.1) for correlations with our outflow-related quantities. The significant correlations between the Fe II and Mg II EW and the SFR surface density discussed above are not present when $\Sigma_{\rm SFR,B}$ is used; we find EW and Δv to be uncorrelated ($\sigma \leqslant 1.9$) with $\Sigma_{\rm SFR,B}$ for both Fe II and Mg II. On the other hand, we observe a 3.5σ correlation between the Mg II maximum outflow velocity and $\Sigma_{\rm SFR,B}$, slightly more significant than the 2.7σ correlation seen above using our optimal aperture method.

The lack of correlation between EW and stellar mass provides further insight into the correlations described above. If the EW is dominated by the ISM component, we would expect to observe an increase in EW with increasing mass and velocity dispersion; as we do not see this increase, we conclude that changes in the Mg II and Fe II EW across the sample are likely to be due more to the outflow component than the ISM. The Mg II and Fe II EW versus SFR correlations we detect are also then likely to be primarily determined by the outflow. We discuss the relative contributions of the ISM and outflow components further in Section 3.1 below.

We also tested subsets of the 22 object sample for correlations between the stellar population parameters and the outflow quantities. In particular, we calculated Spearman correlation coefficients and determined their significance for the 14 object and 6 object subsamples with 1σ and 3σ outflows, respectively. In both cases, no significant correlations ($\sigma \leqslant 2.6$) were detected between any of the quantities, probably due to the small number of objects in these subsets.

Below, we discuss the results from composite absorption-line spectra constructed from low and high subsamples of galaxy physical properties.

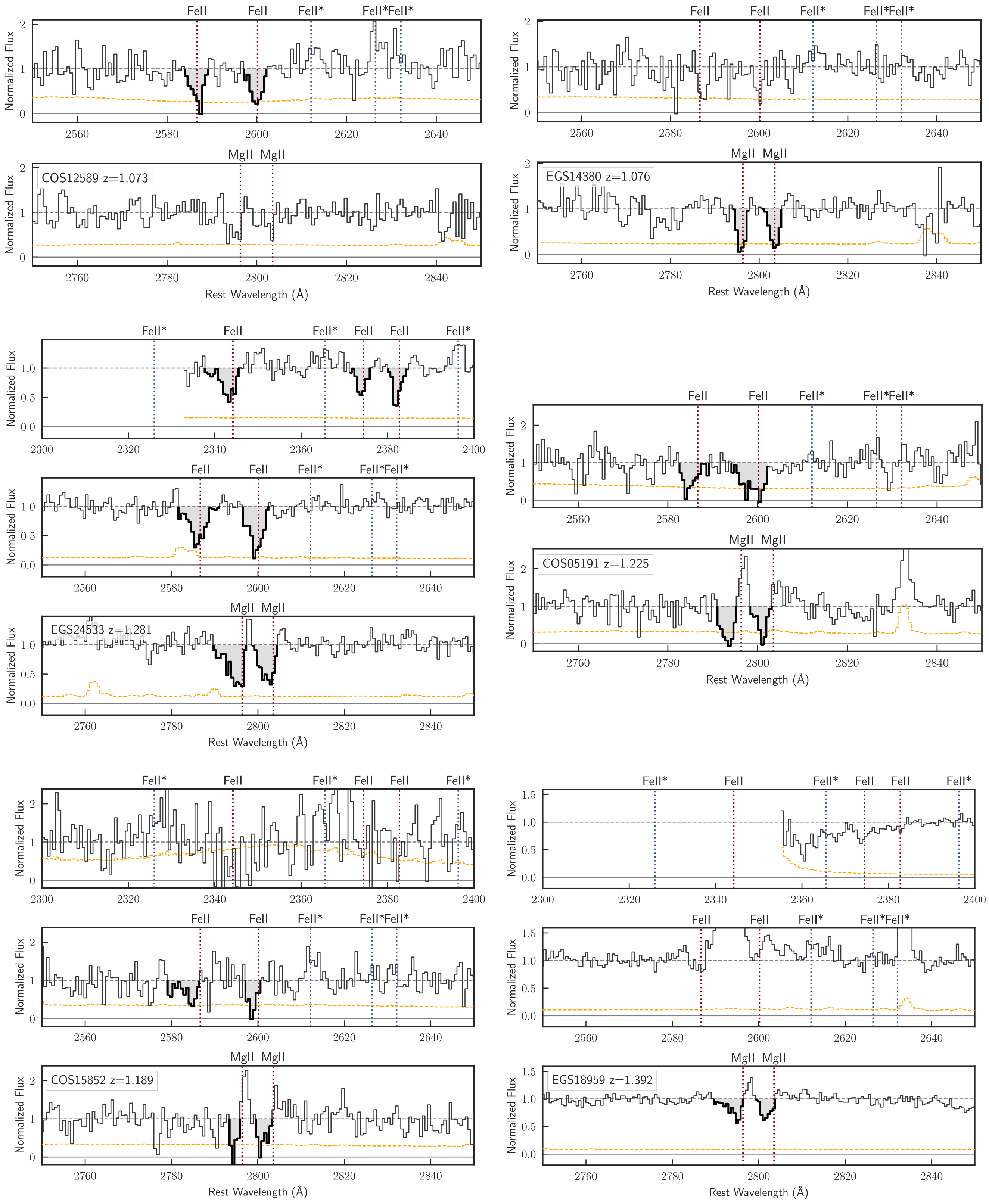

Figure 4. Six representative DEIMOS spectra (dark gray line), with the range over which significantly detected ($\geqslant 3\sigma$) absorption lines are measured overplotted in black and shaded in gray. The orange dashed line shows the total error calculated by summing the statistical and normalization uncertainties in quadrature. In the top two panels, there are only Mg II and Fe II detections. In the left figure of the middle panel, there are many Fe II lines in addition to the Mg II doublet. In the middle right, there is strong Mg II emission-line filling, which occurs significantly in all of the bottom four panels as well. In the bottom row, a noisy spectrum is shown with a correspondingly large error spectrum (especially in the 2300–2400 Å range). On the bottom right, the galaxy has high Mg II S/N but no other lines are detected.

Table 2
Absorption-line Measurements from Keck/DEIMOS

Object	Fe II EW[a] (Å)	Mg II λ2796 EW (Å)	Mg II λ2804 EW (Å)	Fe II Δv[b] (km s^{-1})	Mg II Δv[c] (km s^{-1})	Fe II $v_{\rm max}$[d] (km s^{-1})	Mg II $v_{\rm max}$[e] (km s^{-1})
COS 05191	3.8 ± 0.6	3.1 ± 0.5	2.0 ± 0.5	-96 ± 52	-333 ± 30	-527 ± 56	-612 ± 33
COS 09419	2.5 ± 0.5	1.6 ± 0.4	3.5 ± 0.5	-118 ± 49	-152 ± 34	-432 ± 119	-475 ± 94
COS 10318	⋯	3.3 ± 0.5	3.7 ± 0.5	⋯	-53 ± 51	⋯	-766 ± 189
COS 11696	2.9 ± 0.5	4.0 ± 0.6	3.0 ± 0.4	-136 ± 54	-325 ± 43	-454 ± 79	-825 ± 116
COS 12589	2.4 ± 0.4	⋯	⋯	-8 ± 32	⋯	-378 ± 54	⋯
COS 13739	2.2 ± 0.4	2.4 ± 0.6	3.0 ± 0.7	7 ± 43	-71 ± 82	-268 ± 56	-520 ± 230
COS 14214	3.2 ± 0.2	4.3 ± 0.4	3.6 ± 0.5	1 ± 17	-73 ± 21	-392 ± 49	-614 ± 61
COS 15852	2.1 ± 0.5	1.9 ± 0.5	2.0 ± 0.6	-222 ± 46	-202 ± 28	-494 ± 144	-359 ± 67
COS 16172	2.8 ± 0.4	3.3 ± 0.5	3.6 ± 0.5	69 ± 38	-44 ± 34	-300 ± 70	-416 ± 72
COS 19180	2.2 ± 0.5	⋯	⋯	-9 ± 46	⋯	-294 ± 81	⋯
COS 22785	1.6 ± 0.5	1.5 ± 0.4	⋯	-66 ± 53	-228 ± 46	-423 ± 70	-520 ± 130
COS 25161	2.8 ± 0.7	3.1 ± 0.6	⋯	-278 ± 33	-253 ± 30	-638 ± 42	-557 ± 0
COS 25927	2.3 ± 0.4	1.8 ± 0.4	1.9 ± 0.6	-41 ± 30	-52 ± 38	-288 ± 58	-303 ± 91
COS 27042	4.0 ± 0.5	3.4 ± 1.0	2.9 ± 0.8	-149 ± 27	-223 ± 66	-518 ± 43	-654 ± 175
EGS 02986	2.1 ± 0.7	1.6 ± 0.4	1.8 ± 0.4	87 ± 69	107 ± 26	-295 ± 150	-100 ± 35
EGS 12858	2.0 ± 0.4	2.7 ± 0.6	⋯	78 ± 38	-207 ± 42	-306 ± 42	-534 ± 69
EGS 14380	⋯	1.9 ± 0.4	2.0 ± 0.4	⋯	-35 ± 26	⋯	-297 ± 70
EGS 18959	⋯	1.2 ± 0.2	1.0 ± 0.1	⋯	-262 ± 46	⋯	-760 ± 183
EGS 24533	1.8 ± 0.1	2.9 ± 0.3	2.3 ± 0.2	-79 ± 18	-204 ± 40	-429 ± 51	-756 ± 128
EGS 26680	⋯	2.9 ± 0.4	2.4 ± 0.4	⋯	-82 ± 24	⋯	-442 ± 35
EGS 27539	2.9 ± 0.4	3.8 ± 0.4	3.9 ± 0.4	-51 ± 29	-214 ± 22	-411 ± 35	-565 ± 29
EGS 29026	3.2 ± 0.5	3.2 ± 0.5	4.5 ± 0.5	15 ± 21	-48 ± 42	-249 ± 34	-632 ± 192

Notes.
[a] Weighted average of EWs from all significantly detected Fe II absorption lines.
[b] Weighted average of Fe II centroid velocities from all significantly detected Fe II lines.
[c] Mg II centroid velocities computed using Mg II λ2796.
[d] Weighted average of Fe II maximum velocities from all significantly detected Fe II lines.
[e] Mg II maximum velocities computed using Mg II λ2796.

3.1. Composite Spectra

We created composite spectra by dividing the sample in half by stellar mass, SFR, sSFR, and SFR surface density and constructing the median spectrum of each subsample (we refer to the subsamples as low mass, high mass, low SFR, etc.). The spectra are shown in Figure 8, with error spectra computed from the standard deviations of 100 bootstrap resamples of each subsample. The distributions of the low and high subsets are shown by the blue and red histograms, respectively, in Figure 1. For the low (high) subsamples, we find a median stellar mass of $7.2 \times 10^9\,M_\odot$ ($2.2 \times 10^{10}\ M_\odot$), a median SFR of $5.9\,M_\odot\,{\rm yr}^{-1}$ ($18.1\,M_\odot\,{\rm yr}^{-1}$), a median sSFR of $0.5\,{\rm G\,yr}^{-1}$ ($1.4\ {\rm Gyr}^{-1}$), and a median SFR surface density of $0.23\,M_\odot\,{\rm yr}^{-1}\,{\rm kpc}^{-2}$ ($0.43\,M_\odot\,{\rm yr}^{-1}\,{\rm kpc}^{-2}$). The difference between the medians of the low and high stellar mass, SFR, and sSFR composites is a factor of $\sim$3, while the medians of the low- and high-$\Sigma_{\rm SFR}$ samples differ by a factor of $\sim$2. We also note that the separation between the bins is larger than the uncertainties on the binned quantities by factors ranging from 2.3 (sSFR) to 6.7 (stellar mass).

For each physical quantity, we measured EWs, centroid velocities, and maximum velocities for both of the composite spectra using only the Fe II λ2587, Fe II λ2600, and Mg II $\lambda\lambda$2796, 2804 lines because the lines at redder wavelengths are covered by most (21/22) or all of the individual spectra. We take the weighted average of the Fe II λ2587 and Fe II λ2600 lines for the most direct comparison to the individual spectra. The absorption-line measurements from the composite spectra are reported in Table 3.

To see how the outflow parameters change with galaxy physical properties, we compare the difference in EWs, centroid velocities, and maximum velocities for each low and high subsample (e.g., the Fe II high mass EW versus Fe II low-mass EW). Overall, we see the most significant differences between subsets when measuring the Fe II absorption features, likely because the use of the weighted average of the Fe II λ2587 and Fe II λ2600 lines decreases the uncertainties. In contrast, the Mg II EW and velocity differences between low and high subsamples tend to remain small with respect to the Fe II measurements. This difference may be because we use only Mg II λ2796 for the calculations (as with the individual spectra), which tends to have higher uncertainties with respect to the Fe II weighted averages and is complicated by emission-line filling.

On that note, the most significant difference between the composites is found when comparing the Fe II EWs of the high and low star-formation-related quantities (SFR, sSFR, and $\Sigma_{\rm SFR}$), with the two SFR subsamples showing the largest difference of 1.3 ± 0.3 Å. We find almost no difference between the low- and high-stellar-mass subsets across all three absorption-line measurements, which suggests that the changes in the velocity and EW of the sSFR subsamples are primarily due to changes in the SFR rather than the mass. Excluding the low- and high-SFR subsamples, the Mg II EWs also have differences consistent with zero. These results roughly support the Fe II EW versus SFR correlation as well as the Fe II EW versus $\Sigma_{\rm SFR}$ correlation we found by looking at the individual objects.

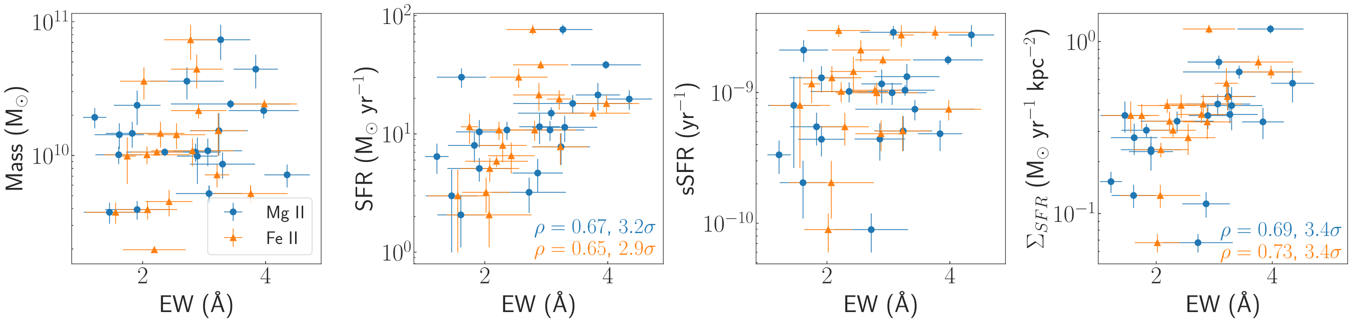

Figure 5. From left to right, we plot the stellar mass, star formation rate, specific star formation rate, and star formation rate surface density against Fe II (orange triangles) and Mg II $\lambda 2796$ (blue circles) equivalent widths. As described in the text, there are significant correlations between the Mg II EW and SFR, Mg II EW and $\Sigma_{\rm SFR}$, and Fe II EW and $\Sigma_{\rm SFR}$, and a marginal correlation between Fe II EW and SFR as well. Spearman correlation coefficients and significances are shown in the plots for which there are significant correlations, color-coded by absorption line.

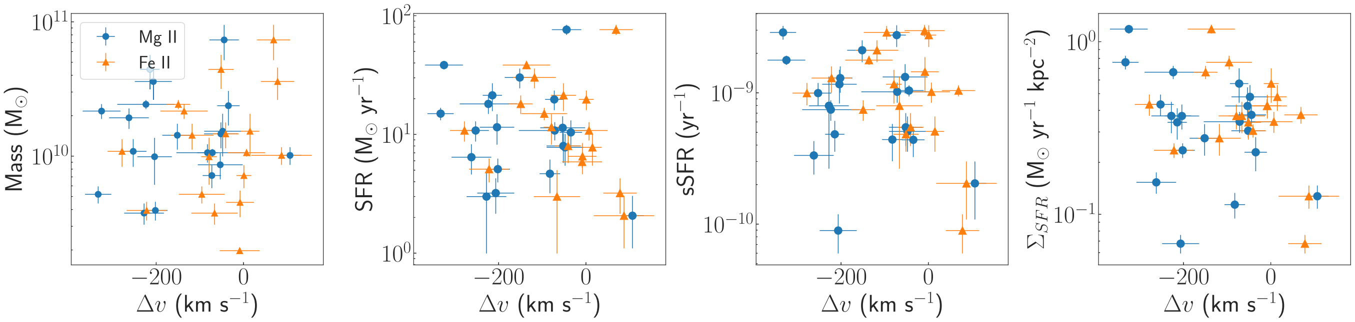

Figure 6. From left to right, we plot the stellar mass, star formation rate, specific star formation rate, and star formation rate surface density vs. the Fe II and Mg II velocity centroids Δv. The symbols are as in Figure 5, and we find no significant correlations between any of the quantities ($\sigma \leqslant 1.4$).

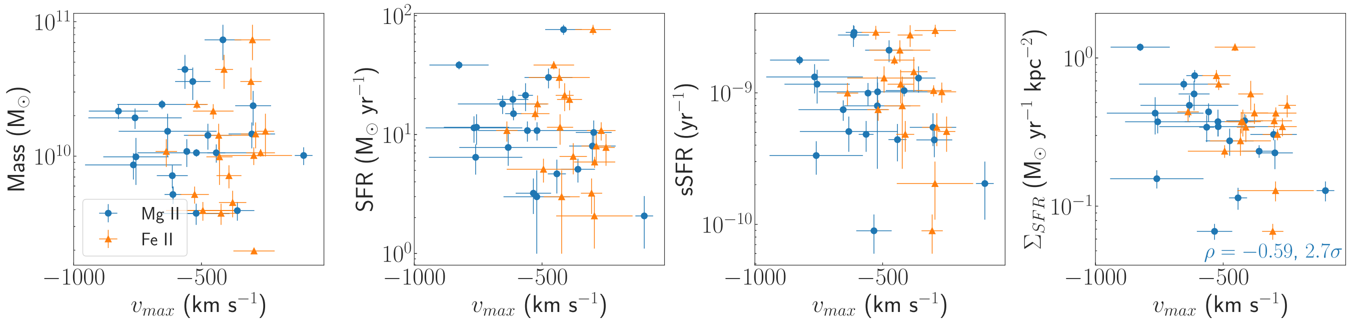

Figure 7. From left to right, we plot the stellar mass, star formation rate, specific star formation rate, and star formation rate surface density vs. the Fe II and Mg II maximum velocity $v_{\rm max}$, defined as the velocity where the absorption line reaches the continuum on the blue side of the line. The symbols remain the same as in Figures 5 and 6. There is a marginal correlation between SFR surface density and Mg II maximum outflow velocity (correlation coefficient and significance shown in the figure), and no other correlations are found ($\sigma \leqslant 1.9$).

In comparing the outflow velocities between the low and high subsamples, we again find that the Fe II measurements vary more between subsamples than the Mg II velocities. The Fe II centroid velocities are consistently faster in all of the high-SFR-related composites, with the largest difference of -77 ± 39 km s^{-1} found between the low- and high-SFR subsamples. We also find a significantly faster Fe II maximum velocity in the high-SFR sample. The only significant velocity-related difference in the Mg II composite measurements is found for the SFR surface densities, for which the centroid velocity is faster in the higher-$\Sigma_{\rm SFR}$ sample.

By looking at the profiles of the composite spectra, we can also try to see how the ISM and outflow components of the Mg II and Fe II absorption lines change between subsamples. In the second row of Figure 8 (the composites based on SFR, which show the largest differences between high and low subsamples), we note that the red wings of the absorption lines have very similar profiles. This suggests that the velocity dispersion of the ISM is similar in the two subsets, although the spectral resolution of ~180 km s^{-1} likely prevents us from fully resolving the ISM component. Larger differences are found on the blue sides of the lines, implying that the difference between the spectra of the two subsamples is largely determined by the outflow component. This, along with the higher covering fractions indicated by the larger depth of the lines throughout the absorption profile in the high-SFR subsample (especially on the blue sides of the lines), points to stronger outflow components associated with higher SFRs.

We summarize our study and discuss the results and future prospects below.

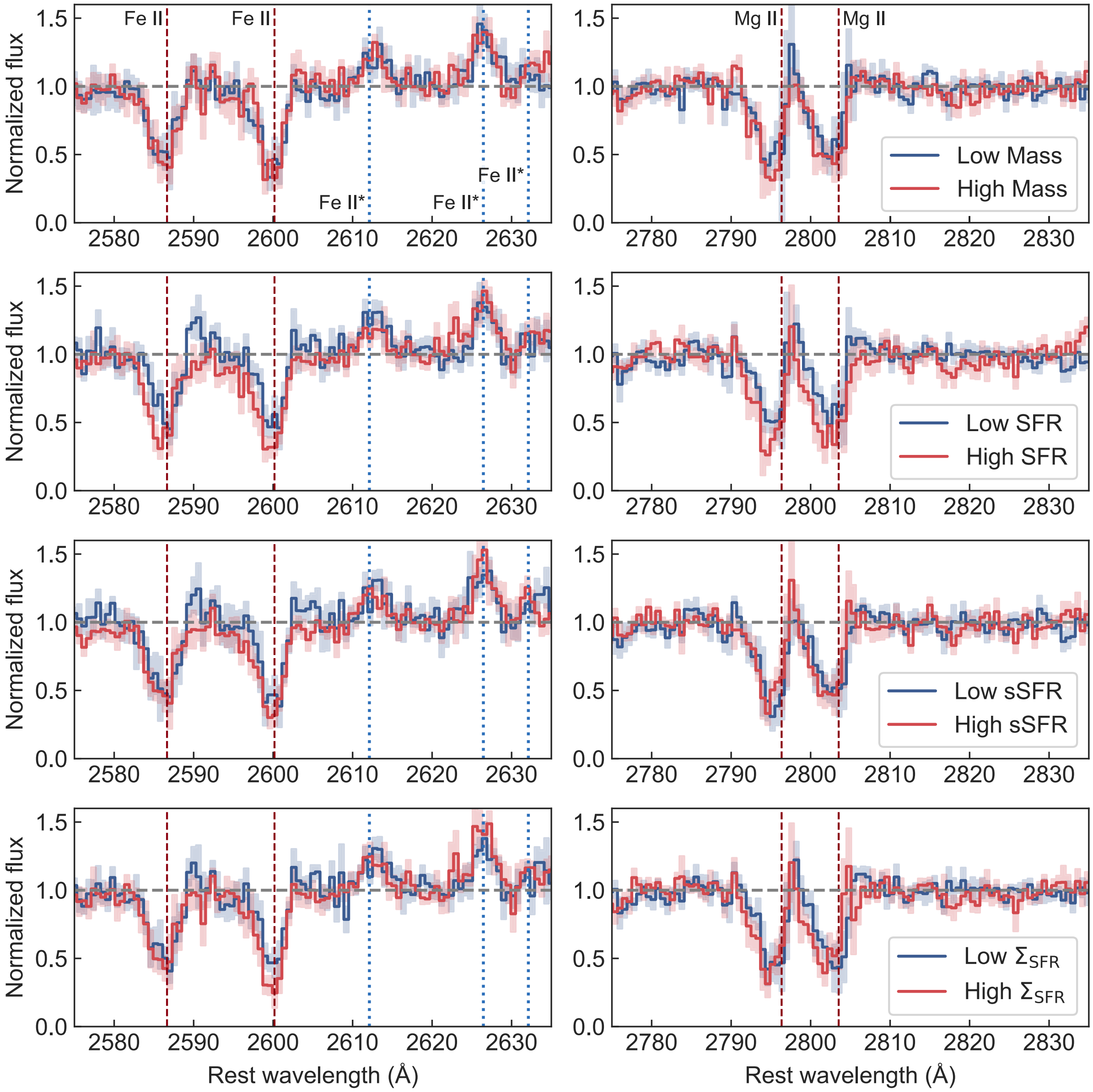

Figure 8. Composite spectra constructed from subsets of galaxies based on the galaxy properties of Figure 1. The left column of panels shows Fe II transitions at ~2600 Å, while the right column shows the Mg II λλ2796, 2804 doublet. From top to bottom, composite spectra are binned by stellar mass, SFR, specific SFR, and SFR surface density. The color scheme is the same as Figure 1, with red and blue corresponding to the low and high respective subsamples of a particular quantity. Uncertainties are shown as faded bars behind the spectra.

4. Summary and Discussion

We have investigated the relationship between galactic outflows and star formation by compiling a joint data set of 22 star-forming galaxies at $1 \lesssim z \lesssim 1.5$ with rest-frame near-UV absorption-line spectra from Keck/DEIMOS and Hα emission-line maps from WFC3/G141 grism spectra taken as part of the 3D-HST survey. All of the objects have at least a 3σ detection of the Hα emission line; 18 have Fe II absorption, and 20 have Mg II significantly detected. The sample has a median mass and standard deviation of $\log(M_*/M_\odot) = 10.2 \pm 0.5$, and a median redshift of 1.22 with a standard deviation of 0.16. Our primary results are enumerated below.

1. We used the grism data and the `Grizli` pipeline to construct 1D and 2D spectra (see Figure 2 for sample 2D spectra) and Hα emission-line maps for each of the 22 objects. We determined the sizes of the regions of strongest star formation from the Hα maps, choosing the area that maximizes the S/N of the integrated Hα flux (Figure 3). We explained this method of area measurement in detail in Section 2.1.1. With the Hα luminosities and sizes, we compute SFRs, sSFRs, and SFR surface densities. These quantities and their respective distributions are listed in Table 1 and plotted in Figure 1.
2. From the DEIMOS spectra, we measured Fe II and Mg II equivalent widths, centroid velocities, and maximum velocities (the velocity where the flux reaches the continuum on the blue side of the line) for each of the objects. These measurements are given in Table 2, and a representative sample of the spectra is shown in Figure 4.
3. The results from the Hα and absorption-line measurements are combined in Figures 5–7, in which we plot stellar mass, SFR, sSFR, and $\Sigma_{\rm SFR}$ against EW, centroid velocity (Δv), and maximum velocity ($v_{\rm max}$), respectively. Spearman

Table 3
Composite Spectra Properties

Composite[a]	Fe II EW[b] (Å)	Mg II λ2796 EW (Å)	Fe II Δv[c] (km s^{-1})	Mg II Δv[d] (km s^{-1})	Fe II $v_{\rm max}$[e] (km s^{-1})	Mg II $v_{\rm max}$[f] (km s^{-1})
Low Mass	2.2 ± 0.2	2.1 ± 0.5	-76 ± 22	-198 ± 46	-498 ± 49	-574 ± 96
High Mass	2.2 ± 0.2	2.3 ± 0.3	-48 ± 20	-179 ± 28	-348 ± 34	-574 ± 32
Low SFR	1.7 ± 0.2	1.7 ± 0.3	-25 ± 18	-173 ± 31	-384 ± 31	-509 ± 32
High SFR	3.0 ± 0.3	2.6 ± 0.3	-102 ± 35	-191 ± 22	-519 ± 66	-574 ± 64
Low sSFR	2.0 ± 0.2	2.3 ± 0.3	-44 ± 22	-156 ± 32	-394 ± 49	-509 ± 64
High sSFR	2.7 ± 0.2	2.2 ± 0.3	-104 ± 30	-200 ± 33	-470 ± 64	-574 ± 96
Low $\Sigma_{\rm SFR}$	1.9 ± 0.2	2.0 ± 0.3	-44 ± 22	-145 ± 28	-422 ± 58	-509 ± 32
High $\Sigma_{\rm SFR}$	2.6 ± 0.2	2.3 ± 0.3	-86 ± 26	-193 ± 25	-467 ± 62	-574 ± 64

Notes.
[a] See Figure 1 for the distributions and ranges of each subsample.
[b] Weighted average of Fe II λ2587 and Fe II λ2600 equivalent widths.
[c] Weighted average of Fe II centroid velocities from Fe II λ2587 and Fe II λ2600.
[d] Mg II centroid velocities computed using Mg II λ2796.
[e] Weighted average of Fe II maximum velocities from Fe II λ2587 and Fe II λ2600.
[f] Mg II maximum velocities computed using Mg II λ2796.

correlation coefficients and their significances are computed for each of the relationships. The Fe II and Mg II EWs are both positively correlated with the SFR surface density at the $\sim 3.4\sigma$ level, and the Mg II EW also increases with the SFR with $\sigma = 3.2$. Marginal correlations are found between the Fe II EW and the SFR ($\sigma = 2.9$), and Mg II maximum outflow velocity versus SFR surface density ($\sigma = 2.7$). There are no significant correlations ($\sigma < 2$) between the other plotted quantities.

4. Composite spectra were formed by splitting the data set into low and high subsamples based on stellar mass, SFR, sSFR, and SFR surface density (Figure 8). For each low and high subset, we measured the Fe II and Mg II EWs, centroid velocities, and maximum velocities (see Table 3). For all of the star-formation-related quantities (SFR, sSFR, and $\Sigma_{\rm SFR}$), the Fe II absorption lines show significantly larger EWs and centroid velocities for the high subsets relative to the low subsamples. We find that the Fe II and Mg II absorption lines in the high-SFR composites have stronger blue wings, supporting the hypothesis that the increase in EW seen with SFR in the spectra of individual objects is due to an increase in the strength of the outflow component with SFR.

Given the complex physics of galactic outflows, many authors have attempted to constrain their driving mechanisms by identifying relationships between galactic properties (e.g., mass, SFR) and outflow-related quantities such as wind velocity. In the local universe ($z \sim 0$), Martin (2005), Rupke et al. (2005), Chisholm et al. (2015), and Heckman et al. (2015) have observed outflows in relatively small ($\sim$50) samples of star-forming galaxies. These samples cover a wide range in mass ($\sim 10^7$–$10^{11}\,M_\odot$) and SFR ($\sim$0.1 to nearly $1000\,M_\odot\,{\rm yr}^{-1}$), and the inclusion of dwarf galaxies with low masses and SFRs has been crucial to the detection of trends between galaxy and outflow properties. Multiple studies have extended these observations to $z \sim 1$ (e.g., Weiner et al. 2009; Rubin et al. 2010, 2014; Kornei et al. 2012; Martin et al. 2012; Bordoloi et al. 2014); however, the higher-redshift samples span only the upper end of parameter space (stellar masses $\gtrsim 10^9\,M_\odot$, SFRs $\gtrsim 110\,M_\odot\,{\rm yr}^{-1}$) and often rely on the coadding of large numbers of spectra.

From these observations, several trends have been detected that link star formation to outflow characteristics. Various studies have detected a shallow increase in outflow velocity with SFR, finding relationships similar to $v \sim {\rm SFR}^{0.3}$ (Martin 2005; Rupke et al. 2005; Weiner et al. 2009; Chisholm et al. 2015; Trainor et al. 2015). Outflow velocities have also been found to generally increase with SFR surface density, both locally (Heckman et al. 2015) and at higher redshifts (Kornei et al. 2012), although this is not always observed (Rubin et al. 2014; Chisholm et al. 2015). Most studies of galactic outflows at $z \sim 1$ have observed correlations between Fe II and Mg II EWs and stellar mass, SFR, or SFR surface density (Weiner et al. 2009; Rubin et al. 2010, 2014; Martin et al. 2012; Bordoloi et al. 2014). Given that the observed Mg II and Fe II transitions are optically thick, the EW is primarily determined by the covering fraction and velocity distribution of the interstellar gas (with a potential additional contribution from emission filling in the case of Mg II). The observed correlations with EW then support a general model in which galaxies with more intense star formation drive outflows with a higher covering fraction to a wider range of velocities.

Our results are consistent with this model and with previous studies at $z \sim 1$ in the sense that the strongest correlations we observe between individual objects are related to the Fe II and Mg II EW, which increase with SFR and SFR surface density. The composite spectra in particular highlight the relationship between star formation and outflows, with larger Fe II EWs and higher velocities seen in the higher subset of all the spectra based on SFR-related quantities. These findings echo previous results at $z \sim 1$ that observe ties between the SFR and SFR surface density and outflow velocity (Kornei et al. 2012; Heckman et al. 2015; Heckman & Borthakur 2016), confirming the close connection between feedback and star formation.

The sample studied here spans slightly more than an order of magnitude in stellar mass, from 2 to $70 \times 10^9\,M_\odot$, and within this relatively narrow range, we find no correlations with outflow properties measured from individual spectra. Most of the composite spectra also show no differences in velocity when divided by mass, although we do find that the Fe II maximum outflow velocity is higher in the low-mass subsample, perhaps contrary to expectations. The lack of a relationship between mass and outflow velocity in the individual objects may be unsurprising given previous findings that these quantities are only weakly correlated (Chisholm et al. 2015; Heckman et al. 2015). The lack of correlation between mass and EW in both the individual and composite spectra may be more unexpected, because most other studies at $z \sim 1$ have observed that the EW increases with stellar mass (Weiner et al. 2009; Rubin et al. 2010, 2014; Kornei et al. 2012; Martin et al. 2012; Bordoloi et al. 2014); however, these studies are based on larger samples covering a wider range in mass.

We can make a more quantitative comparison between our sample and previous results by assuming the scaling relation $v_{\max} \sim \mathrm{SFR}^{0.3}$, as found in previous studies. Using the median values of $v_{\max}$ and SFR in our sample to normalize the relationship, our full range of SFRs then predicts a velocity range of $v_{\max} \sim 250$–700 km s^{-1} across the full sample, much wider than observed; however, two-thirds of our sample lies in the narrower range of $5 < \mathrm{SFR}/(M_\odot\ \mathrm{yr}^{-1}) < 22$, and within this range, the observed scatter in $v_{\max}$ is comparable to the expected variation due to SFR. This suggests that the intrinsic scatter in the velocity–SFR relationship is too large for it to be detected within the range of SFRs probed here. We note that although Heckman et al. (2015) observe a strong correlation between outflow velocity and SFR in the local universe, there is nearly an order of magnitude variation in outflow velocity at a given SFR at the upper end of their sample.

Although our small range of SFRs likely prevents us from finding a correlation between outflow velocity and SFR in the individual objects, we do find a relationship between the Fe II maximum outflow velocity and SFR in the composite spectra that is consistent with previous studies: using the median SFRs for the low- and high-SFR subsets along with their respective maximum velocities, we find that Fe II $v_{\max} \sim \mathrm{SFR}^{0.27}$. Because composite spectra improve the measurement of weak features, the maximum outflow velocity can be measured more robustly, which may explain why this correlation is not seen in the individual objects. We also note that using the Fe II centroid velocities Δv rather than the maximum velocities $v_{\max}$ results in a significantly stronger relationship $\Delta v \sim \mathrm{SFR}^{1.25}$.

Some of the objects in our sample do not follow the general trends between outflow and galaxy properties we have discussed. In particular, we focus on the galaxies that have high SFR surface densities but low outflow velocities. Our data set has four objects (COS 12589, COS 14214, COS 19180, and EGS 29026) that have centroid velocities consistent with zero and SFR surface densities above the sample median of $0.4\ M_\odot\ \mathrm{yr}^{-1}\ \mathrm{kpc}^{-2}$. One possible explanation for this may be that outflows are present, but are collimated and pointed away from our line of sight; evidence for nonspherical outflow geometries has been found in other studies at similar redshifts (Kornei et al. 2012; Martin et al. 2012; Bordoloi et al. 2014; Rubin et al. 2014). If the absence of detectable outflows is an orientation effect, we would expect these four galaxies to be disks observed roughly edge on.

To assess this possibility, we turn to the catalog of structural measurements of CANDELS galaxies (van der Wel et al. 2012), from which we find that these four objects have axis ratios between 0.43 and 0.79, indistinguishable from the rest of the sample. We also find that these four galaxies are compact, all with effective radii below the sample median of 2.6 kpc; however, their SFRs are not particularly high, with all but one below the sample median, meaning that the high SFR surface densities are due more to small sizes than high SFRs. The compact nature of these objects limits our ability to derive constraints on their geometry and orientation, particularly given the fact that the WFC3 F160W images used in the van der Wel et al. (2012) catalog are a factor of ~2 lower in spatial resolution than the ACS F606W and F814W images used by Kornei et al. (2012) and Bordoloi et al. (2014).

While this study is limited by both sample size and dynamic range, it demonstrates the novel combination of direct measurements of star formation at high redshift via Hα emission-line maps and direct measurements of outflows with deep absorption-line spectroscopy. Our sample pushes the limits of current technologies: with existing ground-based facilities, full night integration times (~9 hr) are required to obtain sufficiently high S/N spectra of even bright galaxies at $z \gtrsim 1$, while the time that would be required to obtain space-based Hα maps of galaxies fainter than those in our sample is currently impractical. However, upcoming facilities will enable significant advances in both aspects of this study. The future extremely large telescopes will be able to obtain similarly high-S/N rest-UV spectra of bright galaxies with a fraction of the time, and with longer exposures, they will extend absorption-line studies to fainter or more distant objects.

When the James Webb Space Telescope (JWST) flies, it will conduct deep galaxy surveys at $1 < z < 6$, tracing star formation across ~5 Gyr of cosmic time and looking at earlier and more distant objects than HST is able to see. On board, the Near-Infrared Imager and Slitless Spectrograph (NIRISS) will be analogous to Hubble's WFC3 camera. One of the four NIRISS observing modes enables wide-field slitless spectroscopy over the entire field of view, using one or both of the telescope's grisms and blocking filters to isolate wavelength intervals between 0.8 and 2.2 μm. With JWST's increased collecting area, it will then be possible to map regions of star formation across a broader range of galaxies at $1 \lesssim z \lesssim 2$. JWST and the upcoming 30 m class telescopes will observe galaxies with lower masses and SFRs, correlating outflows and star formation to measure galactic feedback across orders of magnitude in galaxy properties.

The authors thank the referee for a thorough and constructive report, as well as Gabriel Brammer for useful discussions and support with `Grizli`. N.Z.P. was supported by the University of Wisconsin-Milwaukee's Office of Undergraduate Research through the Support for Undergraduate Research Fellows (SURF) Award and Senior Excellence in Research Award (SERA). D.K.E. and N.Z.P. are supported by the US National Science Foundation (NSF) through the Faculty Early Career Development (CAREER) Program grant AST-1255591 and the Astronomy & Astrophysics grant AST-1909198. C.L.M. is supported by NSF grant AST-1817125. The authors wish to recognize and acknowledge the very significant cultural role and reverence that the summit of Maunakea has always had within the indigenous Hawaiian community. We are most fortunate to have the opportunity to conduct observations from this mountain.

Facilities: HST (WFC3/G141), Keck:II (DEIMOS).

Software: `Grizli` (Brammer 2019), `astropy` (The Astropy Collaboration et al. 2013, 2018), `AstroDrizzle` (Gonzaga 2012), DEEP2 Reduction Pipeline (Cooper et al. 2012; Newman et al. 2013).

Appendix
Derivation of the Aperture of Highest Signal-to-noise Ratio

We compute the optimal apertures that maximize the S/N for background-limited sources with Gaussian and exponential surface brightness profiles as referenced in Section 2.1.1 (the optimal radius of a Gaussian profile is a useful quantity for aperture photometry). We assume a two-dimensional circular surface brightness profile with radial form denoted by $g(r)$,

$$g(r) = \begin{cases} \exp\left(-\dfrac{r}{h}\right) & \text{exponential profile} \\ \exp\left(-\dfrac{r^2}{2\sigma^2}\right) & \text{Gaussian profile,} \end{cases} \tag{A1}$$

where h and σ are the scale length and standard deviation of the exponential and Gaussian distributions, respectively. We omit numerical prefactors in Equation (A1), because they do not affect the final result.

The signal $S(R)$ received from the source is the total number of photons collected by the detector, or equivalently, the number of photoelectrons produced. For a source with enclosed area $\mathcal{A}$, $S(R)$ is given by $\int_{\mathcal{A}} g(r)dA$, so for our assumed profiles,

$$S(R) = 2\pi \int_0^R g(r) r\, dr. \tag{A2}$$

The variance of the signal is $S(R)$, assuming Poisson statistics.

The S/N of the observation is then given by the CCD equation (Merline & Howell 1995):

$$S/N = \frac{S(R)}{\sqrt{S(R) + n_{\rm pix}\left(1 + \frac{n_{\rm pix}}{n_B}\right)(N_B + N_D + N_R^2 + G^2\sigma_f^2)}}. \tag{A3}$$

The number of pixels inside the photometric and background apertures corresponds to $n_{\rm pix}$ and n_B, respectively, while the final term in the denominator contains the per-pixel background noise (N_B), dark current (N_D), read noise (N_R), gain in electrons ADU^{-1} (G), and A/D conversion error (σ_f).

We assume that the photometric aperture is small compared to the aperture used to determine the background, thus $n_{\rm pix}/n_B \ll 1$. To simplify the expression, we combine the non-Poisson sources of noise into a single per-pixel noise σ_b. For a circular aperture of radius R, the background variance is then $\pi R^2 \sigma_b^2$, and the total variance is

$$\sigma_{\rm tot}^2 = S(R) + \pi R^2 \sigma_b^2. \tag{A4}$$

This leads to an S/N

$$S/N = \frac{S(R)}{\sqrt{S(R) + \pi R^2\sigma_b^2}} = \frac{2\pi \int_0^R g(r) r\, dr}{\sqrt{2\pi \int_0^R g(r) r\, dr + \pi R^2 \sigma_b^2}}, \tag{A5}$$

which we seek to maximize.

Under the assumption of background-dominated observations, the Poisson noise is negligible compared to the background σ_b, and the S/N is then

$$S/N \approx \frac{S(R)}{\sqrt{\pi R^2 \sigma_b^2}} = \frac{2\pi \int_0^R g(r) r\, dr}{\sqrt{\pi R^2 \sigma_b^2}}. \tag{A6}$$

In order to maximize the S/N, we numerically solve $\frac{\partial (S/N)}{\partial R} = 0$ with the assumption that $S(R) \ll \pi R^2 \sigma_b^2$ for both the exponential and Gaussian profiles. The resulting radii corresponding to the highest S/N apertures are then:

$$R_{\rm max} = \begin{cases} 1.79h & \text{exponential profile} \\ 1.59\sigma & \text{Gaussian profile.} \end{cases} \tag{A7}$$

Note that for the Gaussian profile, $R_{\rm max} = 0.67$ FWHM.

ORCID iDs

Nikolaus Z. Prusinski https://orcid.org/0000-0001-5847-7934
Dawn K. Erb https://orcid.org/0000-0001-9714-2758
Crystal L. Martin https://orcid.org/0000-0001-9189-7818

References

Abramson, L. E., Brammer, G. B., Schmidt, K. B., et al. 2020, MNRAS, 493, 952
Bordoloi, R., Lilly, S. J., Hardmeier, E., et al. 2014, ApJ, 794, 130
Bouche, N., Cresci, G., Davies, R., et al. 2007, ApJ, 671, 303
Bouwens, R. J., Illingworth, G. D., Franx, M., & Ford, H. 2007, ApJ, 670, 928
Brammer, G. 2019, Grizli: Grism Redshift and Line Analysis Software, Astrophysics Source Code Library, ascl:1905.001
Brammer, G. B., van Dokkum, P. G., Franx, M., et al. 2012, ApJS, 200, 13
Brooks, A. M., Governato, F., Quinn, T., Brook, C. B., & Wadsley, J. 2009, ApJ, 694, 396
Calzetti, D., Armus, L., Bohlin, R. C., et al. 2000, ApJ, 533, 682
Chevalier, R. A., & Clegg, A. W. 1985, Natur, 317, 44
Chisholm, J., Tremonti, C. A., Leitherer, C., et al. 2015, ApJ, 811, 149
Cooper, M. C., Newman, J. A., Davis, M., Finkbeiner, D. P., & Gerke, B. F. 2012, spec2d: DEEP2 DEIMOS Spectral Pipeline, Astrophysics Source Code Library, ascl:1203.003
Erb, D. K., Quider, A. M., Henry, A. L., & Martin, C. L. 2012, ApJ, 759, 26
Faber, S. M., Phillips, A. C., Kibrick, R. I., et al. 2003, Proc. SPIE, 4841, 1657
Faucher-Giguère, C.-A., & Quataert, E. 2012, MNRAS, 425, 605
Gabor, J. M., Davé, R., Oppenheimer, B. D., & Finlator, K. 2011, MNRAS, 417, 2676
Genel, S., Fall, S. M., Hernquist, L., et al. 2015, ApJL, 804, L40
Gonzaga, S. 2012, The DrizzlePac Handbook (Baltimore, MD: STScI)
Grenier, I. A., Black, J. H., & Strong, A. W. 2015, ARA&A, 53, 199
Grogin, N. A., Kocevski, D. D., Faber, S. M., et al. 2011, ApJS, 197, 35
Heckman, T. M. 2002, in ASP Conf. Ser. 254, Extragalactic Gas at Low Redshift, ed. J. S. Mulchaey & J. T. Stocke (San Francisco, CA: ASP), 292
Heckman, T. M., Alexandroff, R. M., Borthakur, S., Overzier, R., & Leitherer, C. 2015, ApJ, 809, 147
Heckman, T. M., Armus, L., & Miley, G. K. 1990, ApJS, 74, 833
Heckman, T. M., & Borthakur, S. 2016, ApJ, 822, 9
Hopkins, A. M., & Beacom, J. F. 2006, ApJ, 651, 142
Hopkins, P. F., Cox, T. J., Kereš, D., & Hernquist, L. 2008, ApJS, 175, 390
Hopkins, P. F., Quataert, E., & Murray, N. 2012, MNRAS, 421, 3522
Kennicutt, R. C. 1998, ARA&A, 36, 189
Kereš, D., Katz, N., Weinberg, D. H., & Davé, R. 2005, MNRAS, 363, 2
Koekemoer, A. M., Faber, S. M., Ferguson, H. C., et al. 2011, ApJS, 197, 36
Kornei, K. A., Shapley, A. E., Martin, C. L., et al. 2012, ApJ, 758, 135
Leitherer, C., Schaerer, D., Goldader, J. D., et al. 1999, ApJS, 123, 3
Martin, C. L. 2005, ApJ, 621, 227
Martin, C. L., & Bouché, N. 2009, ApJ, 703, 1394
Martin, C. L., Shapley, A. E., Coil, A. L., et al. 2012, ApJ, 760, 127
Ménard, B., Wild, V., Nestor, D., et al. 2011, MNRAS, 417, 801
Merline, W. J., & Howell, S. B. 1995, ExA, 6, 163
Minchev, I., Martig, M., Streich, D., et al. 2015, ApJL, 804, L9
Momcheva, I. G., Brammer, G. B., van Dokkum, P. G., et al. 2016, ApJS, 225, 27
Murray, N., Ménard, B., & Thompson, T. A. 2011, ApJ, 735, 66

Murray, N., Quataert, E., & Thompson, T. A. 2005, ApJ, 618, 569
Nelson, D., Genel, S., Vogelsberger, M., et al. 2015, MNRAS, 448, 59
Nelson, E. J., van Dokkum, P. G., Förster Schreiber, N. M., et al. 2016a, ApJ, 828, 27
Nelson, E. J., van Dokkum, P. G., Momcheva, I. G., et al. 2016b, ApJL, 817, L9
Newman, J. A., Cooper, M. C., Davis, M., et al. 2013, ApJS, 208, 5
Péroux, C., & Howk, J. C. 2020, ARA&A, 58, 363
Planck Collaboration, Ade, P. A. R., Aghanim, N., et al. 2016, A&A, 594, A13
Prochaska, J. X., Kasen, D., & Rubin, K. 2011, ApJ, 734, 24
Reddy, N. A., Kriek, M., Shapley, A. E., et al. 2015, ApJ, 806, 259
Rix, S. A., Pettini, M., Leitherer, C., et al. 2004, ApJ, 615, 98
Rubin, K. H. R., Prochaska, J. X., Koo, D. C., et al. 2014, ApJ, 794, 156
Rubin, K. H. R., Weiner, B. J., Koo, D. C., et al. 2010, ApJ, 719, 1503
Rupke, D. S., Veilleux, S., & Sanders, D. B. 2005, ApJS, 160, 115
Sales, L. V., Navarro, J. F., Schaye, J., et al. 2010, MNRAS, 409, 1541
Sales, L. V., Navarro, J. F., Theuns, T., et al. 2012, MNRAS, 423, 1544
Salpeter, E. E. 1955, ApJ, 121, 161
Schreiber, N. M. F., Übler, H., Davies, R. L., et al. 2019, ApJ, 875, 21
Shapley, A. E. 2011, ARA&A, 49, 525
Shapley, A. E., Steidel, C. C., & Pettini, M. 2003, ApJ, 588, 25
Skelton, R. E., Whitaker, K. E., Momcheva, I. G., et al. 2014, ApJS, 214, 24
Soto, K. T., Martin, C. L., Prescott, M. K. M., & Armus, L. 2012, ApJ, 757, 86
Speagle, J. S., Steinhardt, C. L., Capak, P. L., & Silverman, J. D. 2014, ApJS, 214, 15
Steidel, C. C., Erb, D. K., Shapley, A. E., et al. 2010, ApJ, 717, 289
Strickland, D. K., & Stevens, I. R. 2000, MNRAS, 314, 511
The Astropy Collaboration, Price-Whelan, A. M., Sipőcz, B. M., et al. 2018, AJ, 156, 123
The Astropy Collaboration, Robitaille, T. P., Tollerud, E. J., et al. 2013, A&A, 558, A33
Trainor, R. F., Steidel, C. C., Strom, A. L., & Rudie, G. C. 2015, ApJ, 809, 89
Tremonti, C. A., Moustakas, J., & Diamond-Stanic, A. M. 2007, ApJL, 663, L77
Übler, H., Naab, T., Oser, L., et al. 2014, MNRAS, 443, 2092
van der Wel, A., Bell, E. F., Häussler, B., et al. 2012, ApJS, 203, 24
van Dokkum, P. G., Brammer, G., Fumagalli, M., et al. 2011, ApJL, 743, L15
Veilleux, S., Cecil, G., & Bland-Hawthorn, J. 2005, ARA&A, 43, 769
Veilleux, S., Maiolino, R., Bolatto, A. D., & Aalto, S. 2020, A&ARv, 28, 2
Wang, W., Faber, S. M., Liu, F. S., et al. 2017, MNRAS, 469, 4063
Wang, X., Jones, T. A., Treu, T., et al. 2019, ApJ, 882, 94
Weiner, B. J., Coil, A. L., Prochaska, J. X., et al. 2009, ApJ, 692, 187
Yabe, K., Ohta, K., Iwamuro, F., et al. 2014, MNRAS, 437, 3647
Zhu, G. B., Comparat, J., Kneib, J.-P., et al. 2015, ApJ, 815, 48